bioRxiv preprint doi: https://doi.org/10.1101/314765; this version posted May 6, 2018. The copyright holder for this preprint (which was not certified by peer review) is the author/funder. All rights reserved. No reuse allowed without permission.

Non-mydriatic chorioretinal imaging in a transmission geometry and application to retinal oximetry

TIMOTHY D. WEBER[1,*] AND JEROME MERTZ[1,2]

[1] *Department of Biomedical Engineering, Boston University, 44 Cummington Mall, Boston, Massachusetts 02215, USA*
[2] *Photonics Center, Boston University, 8 Saint Mary's Street, Boston, Massachusetts 02215, USA*
[*] *tweber@bu.edu*

Abstract: The human retina is typically imaged in a reflection geometry, where light is delivered through the pupil and images are formed from the light reflected back from the retina. In this configuration, artifacts caused by retinal surface reflex are often encountered, which complicate quantitative interpretation of the reflection images. We present an alternative illumination method, which avoids these artifacts. The method uses deeply-penetrating near-infrared (NIR) light delivered transcranially from the side of the head, and exploits multiple scattering to redirect a portion of the light towards the posterior eye. This unique transmission geometry simplifies absorption measurements and enables flash-free, non-mydriatic imaging as deep as the choroid. Images taken with this new trans-illumination approach are applied to retinal oximetry.

OCIS codes: (170.4460) Ophthalmic optics and devices; (170.2945) Illumination design; (170.1470) Blood or tissue constituent monitoring.

References and links

1. R. Poplin, A. V. Varadarajan, K. Blumer, Y. Liu, M. V. McConnell, G. S. Corrado, L. Peng, and D. R. Webster, "Prediction of cardiovascular risk factors from retinal fundus photographs via deep learning," Nat. Biomed. Eng. **2**, 1–7 (2018).
2. C. J. Pournaras, E. Rungger-Brändle, C. E. Riva, S. H. Hardarson, and E. Stefansson, "Regulation of retinal blood flow in health and disease," Prog. Retin. Eye Res. **27**, 284–330 (2008).
3. M. D. Abràmoff, M. K. Garvin, and M. Sonka, "Retinal Imaging and Image Analysis," IEEE Rev. Biomed. Eng. **3**, 169–208 (2010).
4. O. B. Olafsdottir, H. S. Saevarsdottir, S. H. Hardarson, K. H. Hannesdottir, V. D. Traustadottir, R. A. Karlsson, A. B. Einarsdottir, K. D. Jonsdottir, E. Stefánsson, and J. Snaedal, "Retinal oxygen metabolism in patients with mild cognitive impairment," Alzheimer's & Dementia: Diagn. Assess. & Dis. Monit. (posted 1 April 2018, in press).
5. J. K. Lim, Q. X. Li, Z. He, A. J. Vingrys, V. H. Wong, N. Currier, J. Mullen, B. V. Bui, and C. T. Nguyen, "The Eye As a Biomarker for Alzheimer's Disease," Front. Neurosci. **10**, 536 (2016).
6. A. Harris, R. B. Dinn, L. Kagemann, and E. Rechtman, "A Review of Methods for Human Retinal Oximetry," Ophthalmic Surgery, Lasers Imaging **34**, 152–164 (2003).
7. L. E. MacKenzie and A. R. Harvey, "Oximetry using multispectral imaging: theory and application," J. Opt. **20**, 063501 (2018).
8. R. A. Linsenmeier and H. F. Zhang, "Retinal oxygen: from animals to humans," Prog. Retin. Eye Res. **58**, 115–151 (2017).
9. F. C. Delori, E. S. Gragoudas, R. Francisco, and R. C. Pruett, "Monochromatic Ophthalmoscopy and Fundus Photography: The Normal Fundus," Arch. Ophthalmol. **95**, 861–868 (1977).
10. H. Narasimha-Iyer, V. Mahadevan, J. M. Beach, and B. Roysam, "Improved detection of the central reflex in retinal vessels using a generalized dual-Gaussian model and robust hypothesis testing," IEEE Transactions on Inf. Technol. Biomed. **12**, 406–410 (2008).
11. D. A. Salyer, N. Beaudry, S. Basavanthappa, K. Twietmeyer, M. Eskandari, K. R. Denninghoff, R. A. Chipman, and R. I. Park, "Retinal Oximetry Using Intravitreal Illumination," Curr. Eye Res. **31**, 617–627 (2006).
12. D. A. Boas, D. H. Brooks, E. L. Miller, C. A. Dimarzio, M. Kilmer, R. J. Gaudette, and Q. Zhang, "Imaging the Body with Diffuse Optical Tomography," IEEE Signal Process. Mag. **18**, 57–75 (2001).
13. T. N. Ford, K. K. Chu, and J. Mertz, "Phase-gradient microscopy in thick tissue with oblique back-illumination." Nat. methods **9**, 1195–7 (2012).
14. S. L. Jacques and B. W. Pogue, "Tutorial on diffuse light transport," J. Biomed. Opt. **13**, 41302 (2008).
15. ANSI, "American National Standard for Safe Use of Lasers" ANSI Z136.1-2014 (Laser Institute of America, 2014).

bioRxiv preprint doi: https://doi.org/10.1101/314765; this version posted May 6, 2018. The copyright holder for this preprint (which was not certified by peer review) is the author/funder. All rights reserved. No reuse allowed without permission.

16. F. C. Delori, R. H. Webb, and D. H. Sliney, "Maximum permissible exposures for ocular safety (ANSI 2000), with emphasis on ophthalmic devices," J. Opt. Soc. Am. A **24**, 1250 (2007).
17. W. J. Geeraets, R. C. Williams, G. Chan, W. T. Ham, D. Guerry, and F. H. Schmidt, "The Loss of Light Energy in Retina and Choroid," Arch. Ophthalmol. **64**, 606–615 (1960).
18. S. Prahl, "Optical Absorption of Hemoglobin," (1999) `https://omlc.org/spectra/hemoglobin/`.
19. S. B. Reddy and B. N. Chatterji, "An FFT-based technique for translation, rotation, and scale-invariant image registration," IEEE Transactions on Image Process. **5**, 1266–1271 (1996).
20. M. Guizar-Sicairos, S. T. Thurman, and J. R. Fienup, "Efficient subpixel image registration algorithms," Opt. Lett. **33**, 156 (2008).
21. M. Hammer, D. Schweitzer, B. Michel, E. Thamm, and A. Kolb, "Single scattering by red blood cells," Appl. Opt. **37**, 7410–7418 (1998).
22. S. C. Park and R. Ritch, "High resolution in vivo imaging of the lamina cribrosa," Saudi J. Ophthalmol. **25**, 363–372 (2011).
23. S. L. Jacques, "Optical Properties of Biological Tissues: A Review," Phys. Medicine Biol. **58**, R37–61 (2013).
24. F. C. Delori, "Noninvasive technique for oximetry of blood in retinal vessels," Appl. Opt. **27**, 1113–1125 (1988).
25. J. P. de Kock, L. Tarassenko, C. J. Glynn, and A. R. Hill, "Reflectance Pulse Oximetry Measurements from the Retinal Fundus," IEEE Transactions on Biomed. Eng. **40**, 817–823 (1993).
26. D. Schweitzer, M. Hammer, J. Kraft, E. Thamm, E. Königsdörffer, and J. Strobel, "In vivo measurement of the oxygen saturation of retinal vessels in healthy volunteers." IEEE Transactions on Biomed. Eng. **46**, 1454–1465 (1999).
27. D. J. Mordant, I. Al-Abboud, G. Muyo, A. Gorman, A. Sallam, P. Ritchie, A. Harvey, and A. McNaught, "Spectral imaging of the retina." Eye. **25**, 309–320 (2011).
28. S. Chen, X. Shu, P. L. Nesper, W. Liu, A. A. Fawzi, and H. F. Zhang, "Retinal oximetry in humans using visible-light optical coherence tomography [Invited]," Biomed. Opt. Express **8**, 1415–1429 (2017).
29. J. B. Hickam, R. Frayser, and J. C. Ross, "A Study of Retinal Venous Blood Oxygen Saturation in Human Subjects by Photographic Means," Circulation **27**, 375–385 (1963).
30. J. Beach, K. Schwenzer, S. Srinivas, D. Kim, and J. Tiedeman, "Oximetry of retinal vessels by dual-wavelength imaging: calibration and influence of pigmentation," J. Appl. Physiol. **86**, 748–758 (1999).
31. E. Stefánsson, M. L. Wolbarsht, and M. B. I. Landers, "In vivo O2 Consumption in Rhesus Monkeys in Light and Dark," Exp. Eye Res. **37**, 251–256 (1983).
32. R. A. Linsenmeier, "Effects of Light and Darkness on Oxygen Distribution and Consumption in the Cat Retina," The J. Gen. Physiol. **88**, 521–42 (1986).
33. S. H. Hardarson, S. Basit, T. E. Jonsdottir, T. Eysteinsson, G. H. Halldorsson, R. A. Karlsson, J. M. Beach, J. A. Benediktsson, and E. Stefansson, "Oxygen Saturation in Human Retinal Vessels Is Higher in Dark Than in Light," Investig. Opthalmology & Vis. Sci. **50**, 2308–2311 (2009).
34. N. M. Anderson and P. Sekelj, "Light-absorbing and Scattering Properties of Non- haemolysed Blood," Phys. Medicine Biol. **12**, 173–184 (1967).
35. R. F. Spaide, H. Koizumi, and M. C. Pozonni, "Enhanced Depth Imaging Spectral-Domain Optical Coherence Tomography," Am. J. Ophthalmol. **146**, 496–500 (2008).
36. D. A. Roberts, "Analysis of vessel absorption profiles in retinal oximetry," Med. Phys. **14**, 124–130 (1987).
37. S. H. Hardarson, A. Harris, R. A. Karlsson, G. H. Halldorsson, L. Kagemann, E. Rechtman, G. M. Zoega, T. Eysteinsson, J. A. Benediktsson, A. Thorsteinsson, P. K. Jensen, J. Beach, and E. Stefánsson, "Automatic retinal oximetry," Investig. Ophthalmol. & Vis. Sci. **47**, 5011–5016 (2006).

1. Introduction

A wealth of ocular and systemic health information is potentially contained in the optical appearance of the posterior human eye (i.e. fundus) [1]. The retina is an extension of the central nervous system, and as such, possesses a tightly-regulated blood supply similar to that of the brain [2]. Inner retinal circulation transits the optic nerve and overlays the retina, while outer photoreceptors are primarily nourished by the underlying highly-vascularized choroid. Mis-regulation or damage to retinal circulation has been implicated in ocular diseases such as age-related macular degeneration and systemic diseases such diabetes and cardiovascular disease [3]. Recent work has suggested that possible biomarkers for neurodegenerative conditions, like Alzheimer's disease, may also exist in the retinal vasculature [4, 5]. Thus, there is strong need for high-throughput, noninvasive methods to monitor retinal circulation.

Retinal imaging is routinely performed with a fundus camera, which focuses light through the subject's pupil and records images of the light reflected back from the retina. While this method generally provides adequate (qualitative) contrast of major morphological features, such as the vasculature, optic nerve head, and macula, a more quantitative interpretation of

bioRxiv preprint doi: https://doi.org/10.1101/314765; this version posted May 6, 2018. The copyright holder for this preprint (which was not certified by peer review) is the author/funder. All rights reserved. No reuse allowed without permission.

the reflected light is surprisingly difficult to obtain. Based on the spectral differences between absorption of chromophores in the eye, spectroscopic analysis of the reflected images should, in principle, reveal relative distributions of chromophores throughout the fundus. A clinically important application of fundus spectroscopy is retinal oximetry, which seeks to quantify the relative amounts of oxygenated and deoxygenated hemoglobin (HbO_2 and Hb) present in retinal vessels (see Ref. [6] for an excellent introduction to retinal oximetry, or Ref. [7] for a recent comprehensive review of multispectral imaging oximetry). It has repeatedly been shown that in major ocular diseases, retinal vessel oxygen saturation abnormalities precede clinically detectable morphological changes [8].

But quantitative retinal oximetry is quite susceptible to various artifacts related to specular back reflections (reflex). These artifacts obscure the spectral signatures used to detect chromophores. Perhaps the most notorious artifact is central vessel reflex which appears as bright glints near the center of otherwise absorbing vessels [9, 10]. The reflex is more intense for large arteries, and may appear and disappear repeatedly along the length of the vessel, leading to the so-called "rattlesnake" artifact in oximetric maps [7]. The inner limiting membrane and superficial nerve fiber layer (NFL) of the retina also cause a smoothly-varying glare across the fundus, particularly for young eyes. Researchers have gone to extreme lengths to avoid these confounding reflections, even so far as puncturing the eye (of swine) to illuminate the retina from highly-oblique angles [11]; however, this is not practical for routine clinical examinations.

In theory, the stymieing effects of fundus specular reflection could be circumvented by adopting a transmission imaging geometry, although it is not immediately obvious how to achieve such a geometry without resorting to unacceptably invasive methods. The solution proposed here is inspired by several compelling applications that exploit the capacity of near-infrared (NIR) light to readily penetrate the head and probe oxygen saturation dynamics deep inside the brain [12]. Certainly if enough light reaches the brain to enable these applications, then it should also be possible to illuminate the back of the eye with NIR light.

Specifically, we propose an alternative fundus imaging strategy based on light delivered transcranially through the subject's temple. The light diffuses through the bone and illuminates the retina not from the front, as in standard techniques, but rather mostly from the back. As such, images are formed from light *transmitted* through the retina rather than *reflected* from the retina. In this way, the image formation is conceptually similar to that of oblique back-illumination microscopy [13], which is capable of transmission-like phase-gradient and absorption contrast microscopic imaging in thick tissue.

The purpose of this paper is to communicate our preliminary results obtained using this new transmission fundus imaging method. The system design and image processing methods are described in detail. Finally, we present an example of retinal oximetry using the technique.

2. Methods

2.1. Fundus transillumination imaging system

The system consists of illumination and detection subsystems shown together in Fig. 1A and detailed separately below. An example raw transcranial fundus image is provided in Fig. 1B.

2.1.1. Transcranial illumination

According to the theory of diffuse light transport [14], only a small fraction of light available at the temple is expected to deeply penetrate the head and reach the posterior eye. Consequently, a high-power light source is necessary to adequately illuminate the retina and choroid for imaging. Since the source need not be coherent, LEDs represent a cost-effective, scalable means of obtaining hundreds of milliwatts of light power at several wavelengths in the NIR spectrum.

Five different high-power metal core PCB LEDs ranging in center wavelength (λ_{center}) from

bioRxiv preprint doi: https://doi.org/10.1101/314765; this version posted May 6, 2018. The copyright holder for this preprint (which was not certified by peer review) is the author/funder. All rights reserved. No reuse allowed without permission.

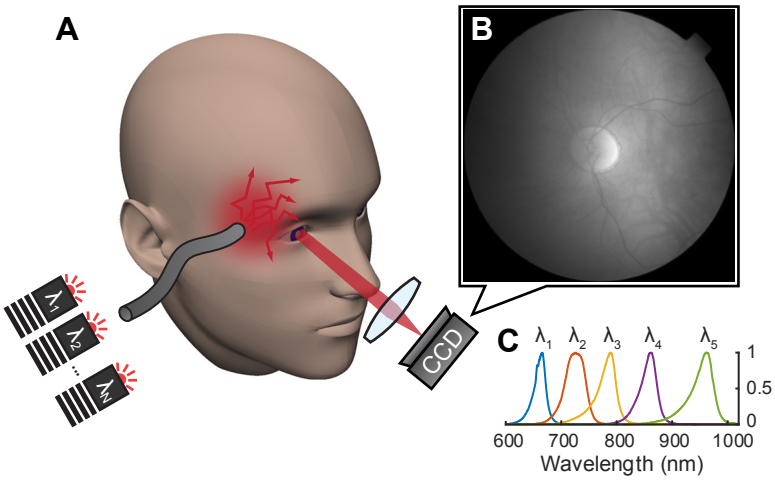

Fig. 1. A: Simplified schematic of a transcranial fundus trans-illumination and imaging system. B: Example raw image recorded on the CCD. C: Normalized measured spectra of available high-power deep red and NIR LEDs.

660 to 940 nm were used to provide transcranial illumination (detailed in Table 1). When active, an LED driver (Thorlabs, LEDD1B) applied the maximum specified current to the particular LED. Resulting spectra for the maximum recommend currents are shown in Fig. 1C. To avoid possible subject discomfort resulting from direct contact with hot LED PCBs, the light was delivered remotely through a flexible fiber bundle (13 mm diam., 36" length). Each LED was imaged onto the proximal end of the fiber bundle via a 3.75x 4f configuration (f_1 = 16 mm, Thorlabs ACL25416U-B; f_2 = 60 mm, Thorlabs LA11340-B). The distal end of the bundle was gently pressed onto the skin near the subject's temple. With careful (3-dimensional) alignment, up to 6 LEDs could be coupled into the bundle, with each LED sharing a portion of the bundle's acceptance cone. In this way, different combinations of LEDs (or several of the same wavelength) could be simultaneously active, however this feature was not used in the present study.

After convergence and transmission through the fiber bundle, a calibrated thermal power meter was used to measure skin irradiance to compare with the ANSI Z136.1 safety standard [15]. The measured irradiances for all wavelengths are below the ANSI Z136.1 maximum permissible exposure (MPE, see Table 1), with the exception of 660 nm, which is equal to the MPE. In calculating skin MPEs, continuous exposure (i.e. >10 sec) was assumed. For exposures <10 sec, the maximum permissible irradiance (in mW/cm^2) is higher. The spectral width at half maximum (FWHM) for each LED was small enough that only the LED center wavelength was considered. Retinal exposure is discussed in a later subsection.

2.1.2. Fundus camera and CCD sensor detection subsystem

A modified Topcon TRC-NW5S non-mydriatic fundus camera (circa 1995) was used to image the trans-illuminated fundus. In the present study, the 45°angle of view setting, corresponding to a 12 mm-circular field of view, was used, though it should be noted that the mirrored aperture of the fundus camera limited imaging to up to 4 mm of pupil diameter. The fundus camera's built-in illumination system was disabled and the dichroic mirror that normally splits observation (NIR) and photography (visible flash) beam paths was removed such that all wavelengths would be sent to the camera port. The original color camera was replaced with a high-sensitivity CCD camera

bioRxiv preprint doi: https://doi.org/10.1101/314765; this version posted May 6, 2018. The copyright holder for this preprint (which was not certified by peer review) is the author/funder. All rights reserved. No reuse allowed without permission.

Table 1. LED choices (with Thorlabs product number), associated ANSI maximum permissible exposures (MPEs) for skin and retina, and measured or estimated irradiance. Retinal MPE is converted from ANSI ocular exposure MPE. Estimation is based on received light power (see text for details). The standard assumes pupil constricts to 3 mm for visible light, and otherwise 7 mm for NIR (hence the jump between 660 and 730 nm retinal MPE).

λ_{center}/FWHM (nm)	Skin exposure (mW/cm^2)		Retina exposure (nW/cm^2)	
	MPE	Measured	MPE	Estimated
660/25 (M660L3)	200	200	110	90
730/37 (M730D2)	230	200	700	220
780/30 (M780D3)	290	120	880	150
850/30 (M850D2)	400	270	1200	550
940/37 (M940D2)	600	200	1700	190

(PCO Pixelfly USB). The camera was operated in "IR boost" mode which enhances the camera's quantum efficiency (QE) in the NIR range (660 nm: 47%, 730 nm: 36%, 780 nm: 26%, 850 nm: 16%, 940 nm: 6%).

To compensate for a resultant intensity gradient from the temporal to nasal side of the fundus, a linear-gradient neutral density filter (Thorlabs, NDL-25C-2) was inserted near an intermediate image plane and intentionally defocused to eliminate the appearance of any dust or structure. The filter was just barely inserted, such that the area of the fundus spanning the dim nasal side to the optic disc did not experience any attenuation. The bright temporal side was attenuated up to a maximum of 50%. The light transmission of the system was measured using a 633 nm HeNe laser, co-aligned with the system's optical axis. Roughly 60% of the beam was transmitted.

2.1.3. Custom GUI and LED toggle

A user interface was written in MATLAB to coordinate and synchronize the illumination and detection subsystems, by way of an Arduino, which was programmed to act as a reconfigurable digital toggle triggered by the camera's exposure-out signal. Thus, the different LED channels were turned on sequentially in synchrony with the camera exposure.

2.1.4. Transcranial retinal exposure and spectral throughput

The ANSI Z136.1 standard assumes hazardous beams will enter the eye through the pupil. Therefore, the standard gives ocular MPEs in terms of power incident on the cornea, which are not directly applicable to transcranial transmission fundus imaging where light primarily exposes the retina from behind. Assuming an "extended source", the ocular MPEs were converted to equivalent retinal irradiances as described previously [16], and listed in Table 1. Similarly, with exposure time, pixel area, sensor QE, fundus camera magnification and transmission, pupil diameter, and published ocular media transmission [17], retinal irradiance could be back-calculated from average pixel value (see Table 1). A Lambertian angular distribution at the retina was assumed, along with a 3 mm-diameter pupil at 660 nm and 4 mm for other LEDs (limited by the fundus camera).

Since LEDs have moderate spectral bandwidth (see Table 1), transmission through skin, bone, and brain is expected to only moderately impact the shape of the spectrum incident on the back of the fundus. This was verified separately by temporarily replacing the camera in our system with a fiber-coupled spectrometer (Thorlabs CCS175 with 1 mm-diameter fiber patch cable). The resultant transmission-responsivity curve (not shown) was used to correct the weighted average absorption coefficient for each chromophore (HbO_2 and Hb) at each LED channel. The weighted

bioRxiv preprint doi: https://doi.org/10.1101/314765; this version posted May 6, 2018. The copyright holder for this preprint (which was not certified by peer review) is the author/funder. All rights reserved. No reuse allowed without permission.

average absorption coefficients in the intermediate wavelength range (730, 780, and 850 nm LEDs) were found to be less sensitive to the correction (<2% change). However, at 660 nm the weighted average absorption coefficients of HbO_2 and Hb were each reduced by 8%. Additionally the weighted average absorption coefficient of deoxyhemoglobin was increased by 26% at 940 nm.

2.2. Subjects and imaging sessions

Four asymptomatic eyes from four normal subjects (23-59 years of age, mean age 46, one female and three males) were imaged. The subjects presented a wide range of choroidal pigmentation, with corresponding (usually correlated) iris colors ranging from blue to brown. For each subject, informed consent was obtained prior to imaging. The research was approved by the Boston University Institutional Review Board.

For each imaging session, the subject fixated on an external target such that the optic disc was centered in the image. Although the system has the capability to temporally interleave LEDs for quasi-simultaneous multispectral imaging, the camera's maximum framerate limited this capability. For instance, enabling three color channels reduced the multispectral framerate to 4 Hz. Because light from the 660 and 730 nm could be weakly perceived, while the others LEDs generally could not, temporal multiplexing of the LEDs effectively caused 4 Hz blinking across the whole field of vision, which was irritating to the subject. Instead, a long series of frames from the same LED were acquired. A 256-frame series was completed in about 26 sec. For one subject (59-year-old white male, moderate pigmentation), a complete multispectral dataset was acquired by repeating this process for all five LED spectral channels. This data was chosen for more detailed spectroscopic analysis and displayed throughout this article.

To ensure that the ANSI-equivalent retinal MPE was not exceeded, the MPE-equivalent maximum allowable pixel value was calculated prior to the start of imaging. Next, the LED current was carefully increased and pixel values were continually monitored to confirm permissible exposure. None of the light conditions used in this study exceeded equivalent retinal MPEs.

2.3. Image processing

Although the use of NIR light permits deep tissue penetration, its major disadvantage is significantly reduced intrinsic absorption contrast, particularly for hemoglobin, which drops precipitously past 600 nm [18]. For example, consider a small 30 μm arteriolar vessel (about the size of the vessel labeled with arrowheads in Fig. 2B & C). The absorption coefficient of highly oxygenated arterial blood at 850 nm is approximately 5.5 cm^{-1}. Light passing through the diameter of the vessel (maximal absorbance) is only attenuated by about 1.6%. With the exposure conditions used to obtain Fig. 2A, an average of 3800 photoelectrons (e^-) per pixel are detected. The expected signal due to the small vessel is thus 61 e^-. In comparison, the rms noise in a shot noise-limited system is 62 e^-, meaning that the signal to noise ratio is no better than unity. Therefore, the vessel cannot be reliably detected with the exposure conditions used for Fig. 2A.

On the other hand, the SNR can be improved by integrating more photons. This is easily achieved by increasing the frame exposure time up to the saturation point, where the number of detected photoelectrons attains the pixel full-well capacity. Very large full-well capacity sensors exist; however, the near-constant eye movement (saccades) encountered in ophthalmic imaging challenges the use of long exposure times. It is thus preferable to record a series of short exposure shot-noise limited frames, register each frame post-hoc, and average the registered frame series in time. The SNR then increases with the square root of the number of frames. This basic strategy was adopted to recover high contrast to noise in trans-illumination fundus imaging.

bioRxiv preprint doi: https://doi.org/10.1101/314765; this version posted May 6, 2018. The copyright holder for this preprint (which was not certified by peer review) is the author/funder. All rights reserved. No reuse allowed without permission.

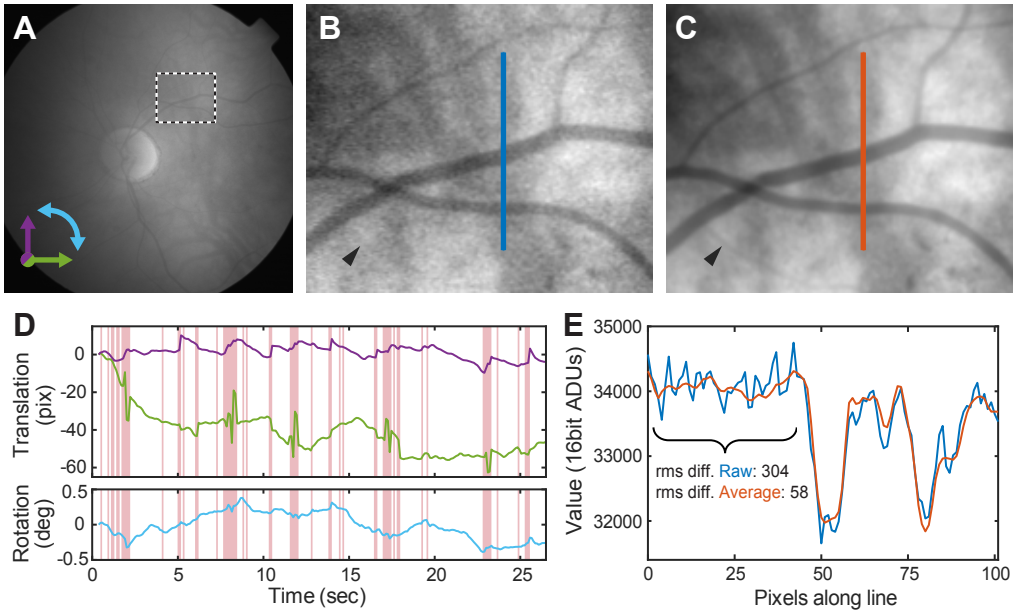

Fig. 2. Averaging registered frames improves low-contrast image quality. A: Single frame from 850 nm LED image series (10 Hz acquisition). B: Magnified view of highlighted region in A. Black/white levels are scaled to the region's min/max values. C: 194-frame average improves SNR, revealing previously undetectable small features (arrowheads in B & C). D: Detected translation (green: X, magenta: Y) and rotation (cyan) for 256-frame series. Motion-corrupted frames (red-background) are excluded from averaging. E: Profiles for lines drawn in B & C, demonstrating SNR improvement. (rms diff.: Root-mean-square pixel to pixel difference)

2.3.1. Image registration and averaging

Custom image registration software was written in MATLAB to register sequential frames to subpixel precision and account for slight rotations from torsional eye movements. Briefly, the algorithm statistically surveys the raw image series and replaces hot pixels with the surrounding non-hot pixel average value. The strategy for rotational and translation registration is based on the work of Reddy and Chatterji [19]. First, the 2D magnitude spectrum of each frame is computed. To reduce the influence of high-frequency noise, an estimate for the circularly-symmetric limit of spatial frequency support is made from the raw frame series. Spatial frequencies beyond the support are systematically excluded by setting them equal to zero. The rotational cross-correlation between pairs of 2D magnitude spectra are computed via the Fourier cross-correlation theorem (i.e. Fourier transforming/inverse transforming along θ in polar coordinates). The shift in the peak of the resulting distribution relative the origin reveals the rotation between frames. The frame series is unrotated by bilinear transformation and the 2D translational cross-correlation is computed between pairs of unrotated frames, with the shift of the 2D peak now revealing the 2D translation. Subpixel translation or rotational precision is obtained by upsampling in the neighborhood of the peak in the cross-correlation as detailed in Ref. [20]. A plot of the detected translational (green: X, magenta: Y) and rotational (cyan) movements versus time for a typical image series is shown in Fig. 2D.

With the exposure duration used in the present study (~100 ms), eye motion inevitably corrupts

bioRxiv preprint doi: https://doi.org/10.1101/314765; this version posted May 6, 2018. The copyright holder for this preprint (which was not certified by peer review) is the author/funder. All rights reserved. No reuse allowed without permission.

a number of frames. The registration software automatically excludes corrupted frames based on the following criteria (shown as red background in Fig. 2D):

- Motion between frames greater than a number of pixels related to the frequency support.
- Multiple peaks were found in the cross-correlation (indicating a quick jump between two positions during one exposure).
- Peak of the cross-correlation was excessively eccentric (indicating motion blur).

After motion exclusion, the stable frames are aligned with bilinear transformation and averaged over time to form a high-SNR single frame. It was assumed that the absorption images were static and that eye movements were not correlated with the cardiac cycle. Therefore, any pulsating effect due the cardiac cycle should be eliminated after averaging over several seconds of video. A comparison between a single frame and the high-SNR average frames is shown in Fig. 2B & C with attendant line profiles plotted in Fig. 2E. No apparent loss of resolution is observed and variation is now limited by the underlying variation of the fundus itself.

2.3.2. Relative absorbance calculation

Absorbance is ordinarily calculated from incident and transmitted light power measurements: $A = -\log(I_{\text{trans}}/I_{\text{inc}})$. As is apparent in Fig. 2A, the illumination for transmission fundus imaging was not spatially uniform. To accurately compute absorbance, the incident power as a function of location must be known. However, determining incident light power behind the imaging focal plane is infeasible because it would require access to behind the choroid and retina. Instead, a relative absorbance is calculated as follows.

First, the high-SNR average image (Fig. 3A) is corrected for slowly-varying global illumination changes by fitting the image to a 3rd degree polynomial surface, avoiding the bright optic disc area by setting weighting parameters to zero within the optic disc. The average image is divided by the fit to produce a flattened image (Fig. 3B). Next the flattened image is local-maximum-filtered, that is, each pixel is replaced with the maximum value in a circular local area around the pixel. The filtered image is smoothed with a Gaussian kernel equal to half the diameter of the local maximum filter, producing Fig. 3C. This smoothed local maximum image is used as a proxy for the incident light power to compute absorbance. In other words, this method calculates absorbance *relative the minimum absorbance* in a local neighborhood around each pixel. Technically, this should be referred to as relative attenuation, a more general term that additionally includes loss due to scattering outside the acceptance angle of the optical system. Such loss may happen, for instance, at blood vessels where erythrocytes are known to cause scattering [21]. However, in subsequent analysis the effect of spatially varying scattering loss is neglected. The assumption is that scattering from the choroid to the cornea is reduced and/or very strongly forward-directed when using NIR light.

3. Results

As predicted, the trans-illumination images in Figs. 2-3 are free from spurious back-reflections, either from the inner limiting membrane or nerve fiber layer (NFL), which, in a conventional reflection-mode imaging, collectively appear as a glare that intensifies towards the optic disc. The images presented here (Fig. 2B & C, especially) are also free from central vessel reflex, or reflections off the curvature of blood vessel walls. Interestingly, the optic disc appears bright compared with the fundus background, possibly due to anisotropic forward scattering parallel the axonal fibers, and also likely due to the absence of underlying choroid and RPE pigment.

The contrast of the relative absorbance image resembles that obtained with fluorescein angiography, since at 850 nm HbO_2 and Hb have similar absorption. The increased brightness of the optic disc relative the surround fundus results in a ring artifact in the processed relative

bioRxiv preprint doi: https://doi.org/10.1101/314765; this version posted May 6, 2018. The copyright holder for this preprint (which was not certified by peer review) is the author/funder. All rights reserved. No reuse allowed without permission.

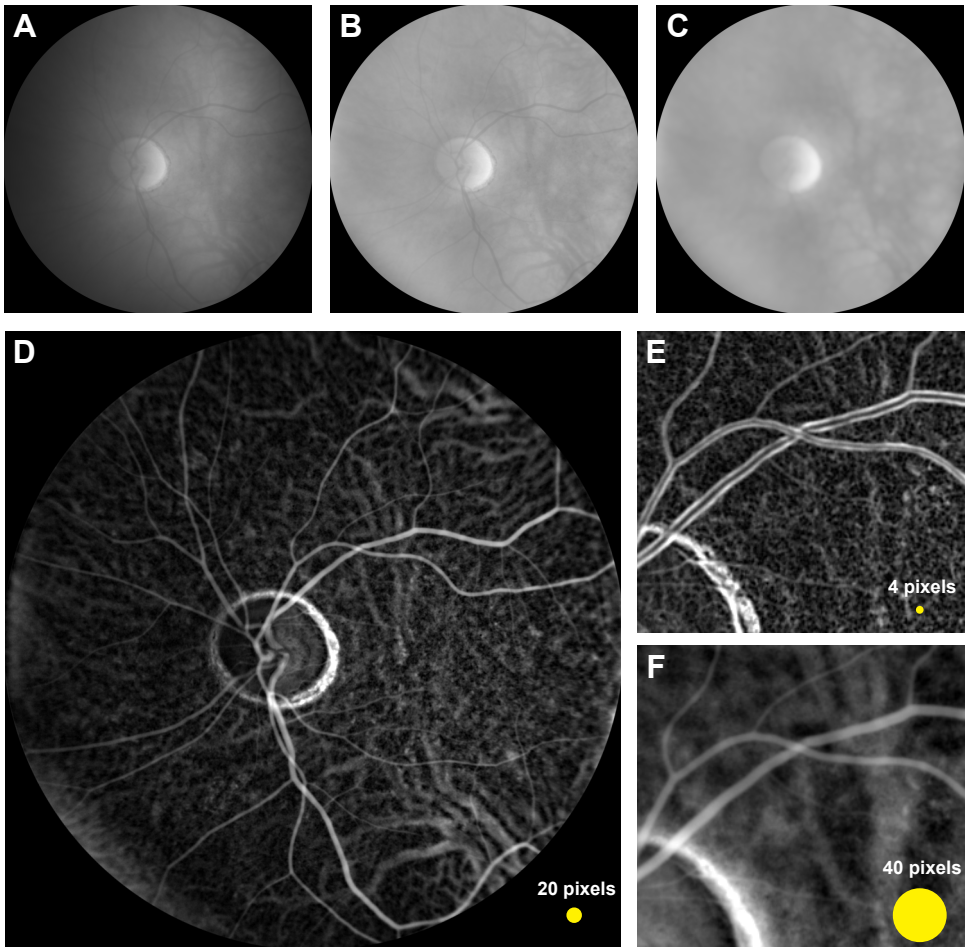

Fig. 3. Left eye from a 59-year old healthy subject. A-D: Relative absorbance calculation with 850 nm trans-illumination (refer to text for details). Yellow circle indicates size of the local maximum filter kernel relative the image. E & F: Effect of changing local maximum filter kernel radius (zoomed region of D). A smaller radius emphasizes sharp changes in absorbance, revealing features such as the lamina cribrosa of the optic disc (E, bottom left) and mottled pigmentation density fluctuations. Larger kernels emphasize larger features such as vessels in the choroid. Animation of steadily increasing kernel radius is provided as Visualization 1.

absorbance image because pixels adjacent the bright disc are assigned erroneously high values during local maximum filtering. In other words, the assumption that the local minimum value can be taken as the incident light power has been violated. More elaborate maximum filtering techniques should be able to compensate for this effect near the edge of the optic disc.

Visibility of certain anatomical features appears to depend on the diameter of the maximum filter kernel used. Namely, a small kernel highlights rapidly varying, tenuous features, tantamount to high-pass filtration because the local-maximum-filtered image over such a small kernel is nearly a low-pass version of the image. Within the optic disc, the bottom left of Fig. 3E, a pattern reminiscent of the collagenous lamina cribrosa is observed [22]. The distinctive mottled appearance of RPE pigment density variations is also apparent in the fundus area [9]. On the other hand, larger kernels emphasize large-scale features, such as choroidal vessels, which are

bioRxiv preprint doi: https://doi.org/10.1101/314765; this version posted May 6, 2018. The copyright holder for this preprint (which was not certified by peer review) is the author/funder. All rights reserved. No reuse allowed without permission.

clearly visible in the background of Fig. 3F.

Notably, there is no visual evidence of the macula, which under visible light fundus photography ordinarily appears as a dark spot 2-3 optic disc diameters temporal the optic disc. The absorbance of macular xanthophylls is evidently negligible for the NIR wavelengths used in this study.

3.1. Multispectral imaging and chromophore unmixing

Data obtained using the other LED channels are processed in a similar way and the resulting relative absorbance images are shown in Fig. 4. As the wavelength of trans-illumination is scanned, two changes are obvious. First, for shorter wavelengths (660 and 730 nm), retinal arteries nearly disappear. This is readily explained by noting that under normoxia, arteries are highly oxygenated, and the absorbance of oxygenated hemoglobin is minimal around 690 nm (see Fig. 5A for complete absorption spectra). Retinal veins contain a mixture of HbO_2 and Hb, which results in significant absorbance across the NIR spectrum. The second notable change is a contrast inversion of the underlying choroidal vessels relative the extravascular choroid. For shorter wavelengths, the choroidal vessels are more weakly absorbing (i.e. appear dark in Fig. 3) than the surrounding patches of the extravascular surroundings. For longer wavelengths (850 and 940 nm), choroidal vessels exhibit greater absorbance (i.e. appear brighter) than the extravascular surroundings. In this case, the extravascular choroid contains melanocytes which, for short wavelengths (660 and 730 nm), are highly absorbing. With increasing wavelength, the absorption of melanin decreases (Fig. 5A, dotted line), while the absorption of oxyhemoglobin increases. Beyond 780 nm, the choroidal vessels exhibit more absorbance than the extravascular melanin-containing choroid, explaining the contrast inversion.

Because the multispectral images were not taken simultaneously, each were registered using manually selected vessel branching points and mapped into a common coordinate system using

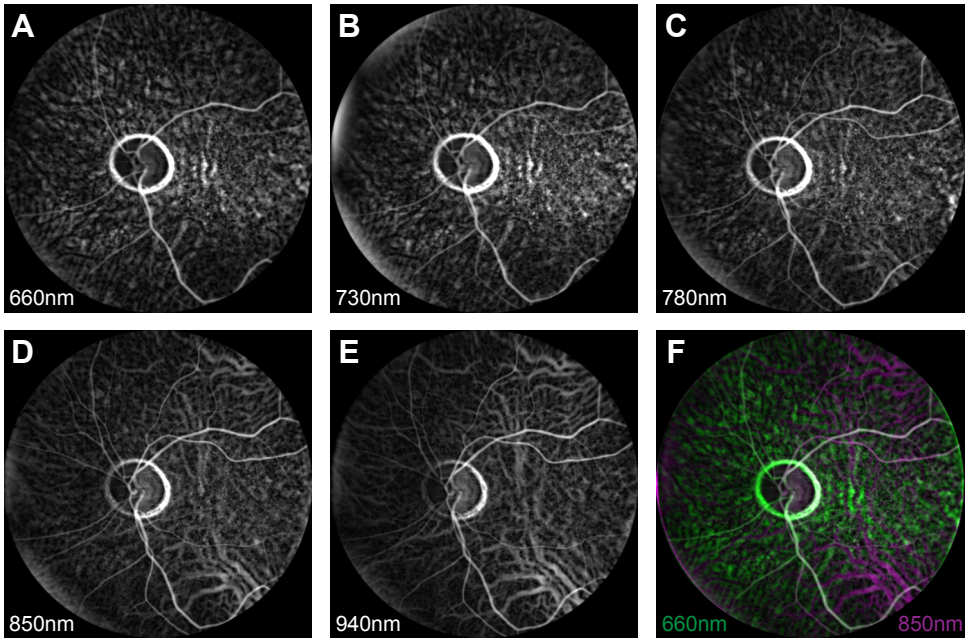

Fig. 4. A-E: Multispectral relative absorbance trans-fundus imaging. Brightness has been autoscaled for clarity. F: 660 and 850 nm images overlaid in false-color for comparison. An animation of the aligned multispectral data is available as Visualization 2.

bioRxiv preprint doi: https://doi.org/10.1101/314765; this version posted May 6, 2018. The copyright holder for this preprint (which was not certified by peer review) is the author/funder. All rights reserved. No reuse allowed without permission.

similarity transforms. Two registered relative absorbance images, which exhibit both contrast changes mentioned above, are shown together in false color in Fig. 4F.

Additionally, with registered multispectral images, one can "unmix" the relative contributions from individual chromophores to the total observed absorbance. According to the Beer-Lambert law, absorbance from multiple chromophores adds linearly with concentration. Thus, a system of equations relating chromophore concentration to absorbance may can be written. The coefficients are equal to the weighted-average absorption coefficients for each chromophore over each LED spectrum, with additional corrections for head transmission and quantum efficiency, as explained above. The system of equations is solved for multispectral data at each pixel using either a pseudo-inverse or a non-negative least squares optimization routine, the latter applying a positivity constraint to the estimated chromophore concentrations. Results for non-negative least squares-based unmixing for HbO_2 and Hb are shown in Fig. 5B. The 940 nm channel was not included due to uncertainty in the large 26% weighted-average absorption coefficient correction for deoxyhemoglobin. The deoxyhemoglobin channel (cyan) in Fig. 5 likely contains some contributions from melanin in the extravascular space of the choroid because the spectral shape of deoxyhemoglobin and melanin are similar. However, incorporating melanin as a third chromophore component yielded poor results (not shown), likely due to the lack of a well-defined spectral difference between melanin and deoxyhemoglobin.

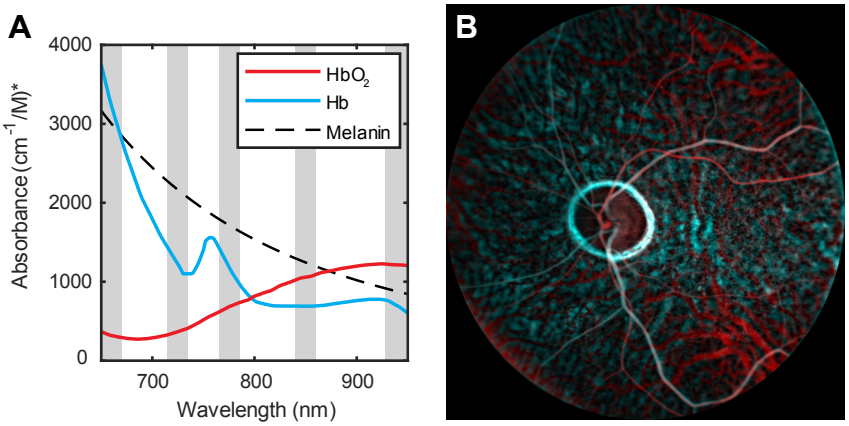

Fig. 5. A: The absorption spectra for the three dominant NIR chromophores of the eye. Gray background indicates available LED channel. B: Oxy- and deoxyhemoglobin (HbO_2 and Hb) distributions based on absorption spectra in A and non-negative least squares spectral unmixing, using 660-850nm relative absorbance images. Hemoglobin spectra obtained from Ref. [18] and average Melanin slope from [23]. (*Melanin plotted in arbitrary units for comparison to hemoglobin spectra)

3.2. Retinal oximetry

With estimates for HbO_2 and Hb concentration, oxygen saturation, $SO_2 = [HbO_2]/([Hb] + [HbO_2])$ may be readily calculated. For a quantitative comparison with results from previous retinal oximetry studies, oxygen saturation from retinal vessels must be isolated from the influence of the choroidal background, which can be quite significant for NIR trans-illumination. Relative to the retinal vessels, the background is generally slowly-varying, (i.e. only the largest choroidal vessels are visible). Thus the background may be numerically estimated using an image restoration technique known as inpainting. For this study, a simple inpainting algorithm that is included in

bioRxiv preprint doi: https://doi.org/10.1101/314765; this version posted May 6, 2018. The copyright holder for this preprint (which was not certified by peer review) is the author/funder. All rights reserved. No reuse allowed without permission.

MATLAB was used. Essentially the algorithm interpolates unknown pixel values based on the solution to Laplace's equation subject to 2D discrete boundary conditions given by the value of the surrounding pixels. The process is graphically illustrated in Fig. 6A. First, clearly delineated vessels are manually-segmented from HbO_2 and Hb maps. Pixels within segmented vessels are set to zero. The background is estimated with inward interpolation (inpainting). Finally, the background-estimated image is subtracted from the original chromophore image, which removes substantial variation and offset introduced by the choroidal background.

For retinal oximetry, a larger local maximum filter kernel (32 pixels) was used for the relative absorbance calculation and least squares was used for spectral unmixing. These tended to produce a more smoothly-varying background for which the background removal strategy outlined above performed well. Several large branching retinal arteries and veins were segmented and background-corrected. Veins over the optic disc exhibited mild spontaneous venous pulsation causing blurring in the high-SNR average image. These veins segments were therefore excluded from oximetric analysis. The corrected vessel maps were smoothed using a low pass filter (Gaussian, 32-pixel FWHM), to remove disruptions near vessel intersections. Estimated SO_2 is overlayed in pseudo-color onto a map of total hemoglobin concentration and shown in Fig. 6B.

Additionally, the mean and standard deviation of SO_2 were computed for different anatomical regions around the optic disc and summarized in Table 2. The arteriovenous (A-V) SO_2 difference is also given for each region, as a relative indicator of local oxygen extraction and metabolic demand. The combined average SO_2 was 89% for arteries and 57% for veins (32% A-V difference).

Table 2. Quantified retinal oximetry results (% oxygen saturation, SO_2) in regional quadrants and across the whole fundus shown in Fig. 6 (temporal: right, superior: top).

Anatomical region	SO_2 mean ± S.D. (# pixels)		A-V difference
	Arterial	Venous	
Superior temporal	88 ± 5 (6849)	64 ± 4 (5539)	24
Superior nasal	92 ± 6 (3229)	48 ± 7 (2543)	44
Inferior nasal	93 ± 4 (1097)	39 ± 3 (1404)	54
Inferior temporal	87 ± 6 (4877)	58 ± 5 (7139)	29
Combined	89 ± 6 (16,761)	57 ± 9 (16,625)	32

4. Discussion

Compared with prior work, the calculated retinal arterial and venous SO_2 oxygen saturation values appear reasonable. Previously, for arterial SO_2, Delori reported 98% using a scanning three-visible wavelength approach [24]. De Kock et al. reported 97% with a time-resolved whole fundus pulse oximeter [25]. Hyperspectral approaches yielded 92% [26] and 104% [27], and recently visible light OCT reported an average across subjects of 92% [28]. For venous SO_2, Hickam et al. reported 59% at the optic disc using a two-color photographic method [29]. Delori reported 45% [24]. Beach and colleagues used a digital two-color imaging method to calculate 55% after correcting for pigmentation and vessel diameter effects [30]. Hyperspectral techniques yielded 35% [27] and 58% [26], while an average of 77% was found using visible light OCT [28].

In this study, the nasal quadrants exhibited greater A-V differences. Interestingly, this is contrary to the findings of Schweitzer et al. [26], who reported a statistically significant increase in A-V difference in the inferior temporal quadrant compared with the inferior nasal quadrant. Since retinal oxygen consumption is greater in darkness in monkey [31] and cat [32], with strong

bioRxiv preprint doi: https://doi.org/10.1101/314765; this version posted May 6, 2018. The copyright holder for this preprint (which was not certified by peer review) is the author/funder. All rights reserved. No reuse allowed without permission.

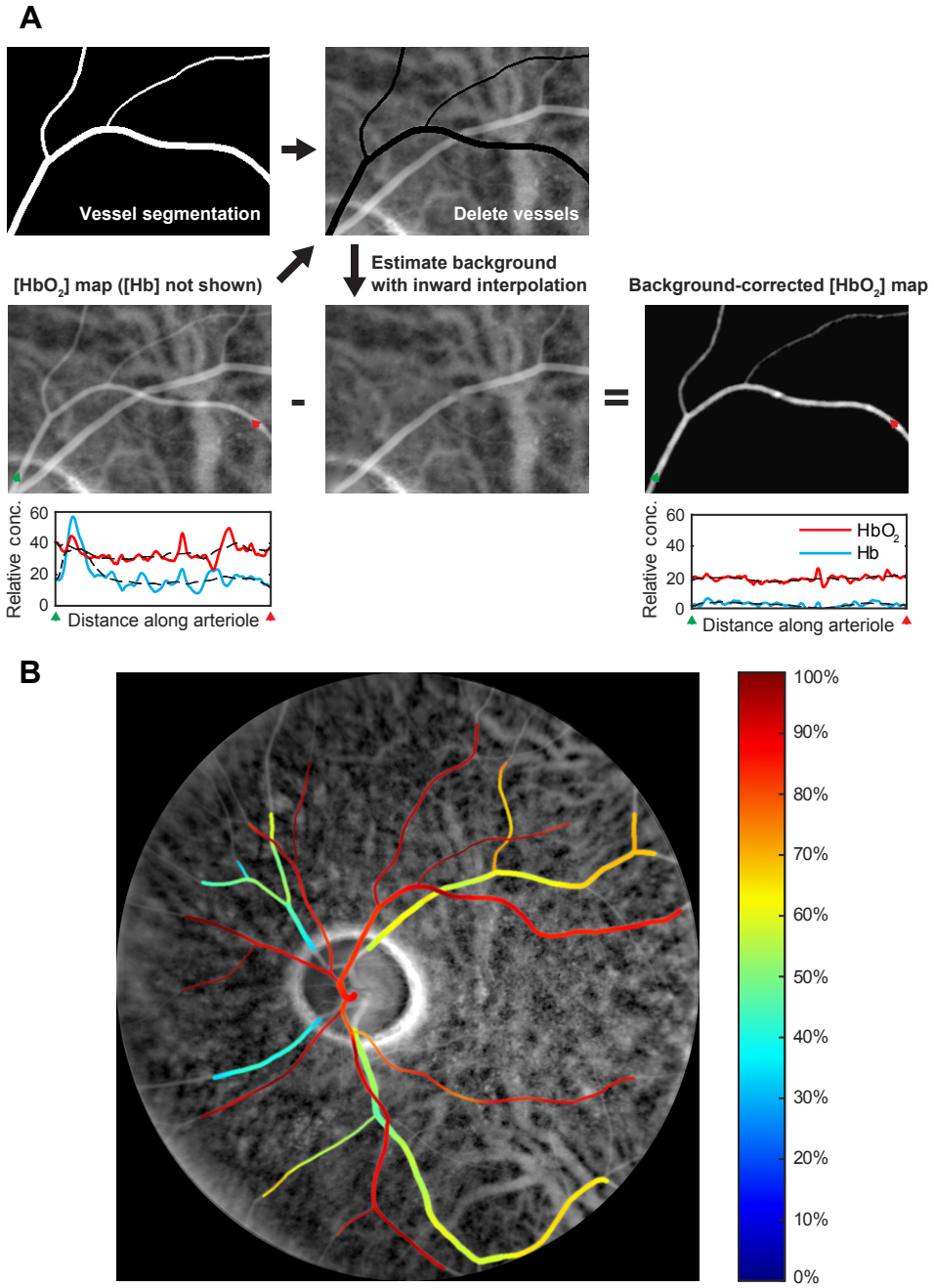

Fig. 6. Retinal oximetry in fundus of the left eye of a normal volunteer. Input data is least squares spectrally unmixed HbO_2 and Hb relative absorbance images. A: Processing steps leading to background-corrected vessel chromophore maps (refer to text for explanation). B: Pseudo-color overlay of oxygen percent saturation (SO_2) in major retinal vessels.

bioRxiv preprint doi: https://doi.org/10.1101/314765; this version posted May 6, 2018. The copyright holder for this preprint (which was not certified by peer review) is the author/funder. All rights reserved. No reuse allowed without permission.

evidence pointing towards the same trend in humans [33], one possible explanation might be that the nasal regions of the trans-illuminated retina, which are farther away from the diffuse light source, are exposed to less light, thus their oxygen consumption is increased relative to the temporal side. This effect would only be significant for the 660 and 730 nm LED channels, however these channels play an outsized role in spectral unmixing due to the large difference in absorption over this range between HbO_2 and Hb. More trans-illumination imaging data is needed to confirm the existence of this relation.

It should be stressed that the oximetric results presented here were obtained without external calibration and instead used only the published extinction coefficients for HbO_2 and Hb. An external calibration is time-consuming, but useful in accounting for attenuation or spurious back-reflections due to tissue scattering. In this study, it was assumed that NIR light was weakly and predominantly forward-scattered, which is a generally valid for biological tissue [23]. Thus, local attenuation due to spatially-varying scattering (i.e. at blood vessels) was ignored and relative concentrations of oxy- and deoxyhemoglobin were simply calculated according to the Beer-Lambert law. This assumption is probably not absolutely true since it is known that whole blood deviates from Beer-Lambert due to multiple scattering at optical depths of a few millimeters [34]. Likely, the attenuation due to scattering has a spectral dependence similar to the absorption of deoxyhemoglobin, and thus may falsely contribute to the unmixed deoxyhemoglobin. This could explain why the average arterial SO_2 determined here is somewhat lower than previous results and also why incorporating melanin into the spectral unmixing led to unsatisfactory results. Monte Carlo simulations of fundus trans-illumination may provide useful insights and help resolve the question of scattering attenuation in this new geometry. Certainly more sophisticated models which take into account wavelength-dependent scattering from spatially-varying features could be adopted, however this is beyond the scope of this preliminary methodology paper.

Another obvious question concerns the validity of spectroscopy obtained over the course of a few minutes. Because the camera's low framerate prevented temporally-interleaved multispectral imaging, the different LED channels were recording sequentially over a total period of 2 minutes. It is possible that vessel oxygenation can vary over this time period, however Hickham and colleagues have found little SO_2 variation over this time period [29], so such dynamics may indeed be safely neglected.

Compared with reflection-based imaging, trans-illumination fundus imaging offers several unique advantages. First, imaging penetration is deep, meaning that discrete choroidal vessels are easily resolved. This is due to a combination of the NIR wavelengths used, which are absorbed and scattered weakly in the inner retina, and the absence of spurious back-reflections, which can easily overwhelm weak signal emanating from deeper structures. Trans-illumination thus has the potential to be a routine, high-throughput alternative to OCT-based approaches [35] for deep choroidal imaging.

Second, trans-illumination ensures that all light detected has traversed the tissue or vessel of interest. This has important implications for retinal oximetry, where vessel surface reflections are a common confounding factor [6]. Researchers have attempted to eliminate these reflections either by fitting the wings of the vessel profile to a Gaussian model [36] or by choosing to analyze only the darkest point along the profile [37]. Both of these techniques reduce the sensitivity because they essentially discard possible data points. In contrast, trans-illumination is free from surface reflections and may utilize the entire vessel profile for oximetric calculations.

The proof-of-concept system detailed here is far from optimized. The SNR, or more precisely the absorption contrast to noise ratio, is primarily limited by shot noise, which is fundamentally linked to the number of photoelectrons generated in the camera sensor. The adoption of newer CMOS sensors, which feature higher NIR sensitivity (up to 2.5x greater at 850 nm) and faster readout times, will increase the number of possible detected photoelectrons. As indicated in Table 1, there is also the possibility of using more power, by adding several of the same LED and/or

bioRxiv preprint doi: https://doi.org/10.1101/314765; this version posted May 6, 2018. The copyright holder for this preprint (which was not certified by peer review) is the author/funder. All rights reserved. No reuse allowed without permission.

spreading the incident light over a larger area of skin. Illumination from other locations, such as the palate or nose may also offer improved or complementary trans-illumination efficiency. For longer wavelengths, significantly more power may be used before reaching ANSI retinal-equivalent MPEs (>8x more for 940 nm). This is fortunate since the quantum efficiency of silicon-based cameras decreases sharply in this spectral range. Since our aim is to demonstrate fundus trans-illumination on a clinically-compatible platform, the current system was designed around a commercial non-mydriatic fundus camera. However, the fundus camera optics limit detection to just 4 mm of pupil diameter. If the fundus camera is replaced with a system capable of utilizing the entire pupil for detection, light throughput for NIR wavelengths is expected to increase by a factor of roughly 4.

5. Conclusion

An alternative illumination method for human non-mydriatic fundus imaging has been presented. It is based on the transcranial delivery of NIR light and on multiple scattering to redirect a portion of this light to the posterior eye, resulting in glare-free retinal imaging. The use of NIR light enables trans-illumination, however at the expense of absorption contrast. We showed that with careful image processing and registration the contrast to noise ratio may be rendered adequate for oximetry measurements. Compared with conventional reflection-based fundus imaging techniques, NIR trans-illumination simplifies absorption measurements and allows imaging deep into the choroid. Importantly, the trans-illumination technique is compatible with reflection-based techniques and we have shown that it works well with a commercial fundus camera. Combining information from these two illumination approaches may improve spectroscopic analysis of the fundus.

Funding

Boston University Photonics Center

Acknowledgments

The authors are indebted to Thomas Bifano and the Boston Micromachine Corporation for providing the fundus camera used in this study. TDW also wishes to thank David Boas and Charles Lin for helpful discussions and encouragement.

Disclosures

The authors declare that there are no conflicts of interest related to this article.